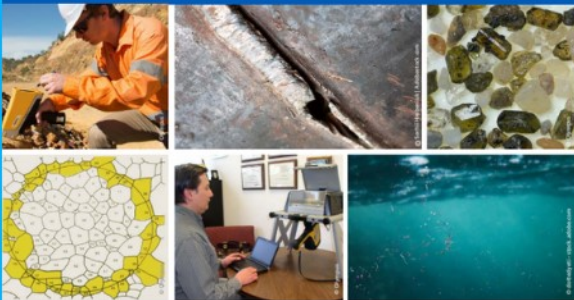




# 2<sup>nd</sup> Advanced Optical Metrology Compendium

## Advanced Optical Metrology

Geoscience | Corrosion | Particles | Additive Manufacturing: Metallurgy, Cut Analysis & Porosity



**EVIDENT**  
**OLYMPUS**

**WILEY**

The latest eBook from **Advanced Optical Metrology**.  
Download for free.

This compendium includes a collection of optical metrology papers, a repository of teaching materials, and instructions on how to publish scientific achievements.

With the aim of improving communication between fundamental research and industrial applications in the field of optical metrology we have collected and organized existing information and made it more accessible and useful for researchers and practitioners.

**EVIDENT**  
**OLYMPUS**

**WILEY**

# Lateral and Vertical Morphology Engineering of Low-Symmetry, Weakly-Coupled 2D ReS<sub>2</sub>

Ping Hu, Hui Zhang, Aolin Li, Liping Sheng, Junjie Jiang, Yue Yu, Wenqiang Huang, Shouheng Li, Han Huang, Jinshan Yu, Haifeng Cheng, Liqiu Mao, Shanshan Wang,\* Fangping Ouyang,\* and Jin Zhang\*

Morphology significantly affects material's electronic, catalytic, and magnetic properties, especially for 2D crystals. Abundant achievements have been made in the morphology engineering of high-symmetry 2D materials, but for the emerging low-symmetry ones, such as ReS<sub>2</sub>, both the morphology control technique and comprehension are lacking. Here, the lateral shape and vertical thickness engineering of 2D ReS<sub>2</sub> by tailoring the growth temperature and the substrate symmetry using chemical vapor deposition, is reported. The temperature increase induces an isotropic-to-anisotropic transition of domain shapes, as well as a monotonic decrease of the domain thickness, which promotes the electrocatalytic performance. The substrate rotational symmetry determines the shape anisotropy of polycrystalline ReS<sub>2</sub> monolayers via a diffusion-limited mechanism, leading to highly oriented square, triangular, and strip-like domains synthesized on the fourfold symmetry SrTiO<sub>3</sub> (001), threefold symmetry c-sapphire, and twofold symmetry a-sapphire substrates, respectively. Various stacking configurations in bilayers are unclosed at the atomic scale. Some are predicted to adopt a type-II band alignment with great potential in photovoltaics. The results give insights into the morphological engineering of a unique class of 2D material with low in-plane lattice symmetry and weak interlayer coupling, which are crucial for their high-quality synthesis and industrial applications.

and a high proportion of surface and edge atoms. On the one hand, the in-plane shape of a 2D domain determines the percentage of edge atoms, which can exhibit special electronic structures and spin states,<sup>[1]</sup> thus leading to unique electrocatalytic,<sup>[2]</sup> luminescent,<sup>[3]</sup> and magnetic performances.<sup>[4]</sup> On the other hand, the vertical morphology engineering, including the domain thickness and the interlayer stacking at the atomic scale, can result in the indirect-to-direct band structure transition,<sup>[5]</sup> unconventional superconductivity,<sup>[6]</sup> ferroelectricity,<sup>[7]</sup> and superlubricity.<sup>[8]</sup>

Tremendous efforts have been devoted to tailoring the in-plane and vertical morphology of high-symmetry 2D materials (e.g., graphene, h-BN, 2H-MoS<sub>2</sub>, and 2H-WS<sub>2</sub>) by the chemical vapor deposition (CVD) method, which is regarded as one of the most promising strategies for the mass production of high-quality and atomically thin films. Various compact shapes (e.g., hexagon, triangle, rectangle, ribbon, etc.), dendritic patterns and thickness-tunable domains have been achieved by means


of substrate engineering, precursor concentration and growth temperature adjustment, post-etching process, etc.<sup>[9–13]</sup> However, the morphology engineering of low-symmetry 2D materials is very limited, resulting in an incomplete comprehension of both the morphology control technique and mechanism.

## 1. Introduction

The properties of materials are significantly affected by morphology. This is especially prominent for 2D materials, whose exotic performance is largely derived from the atomic thickness

P. Hu, H. Zhang, J. Jiang, W. Huang, S. Li, J. Yu, H. Cheng, S. Wang  
Science and Technology on Advanced Ceramic Fibers and Composites Laboratory  
College of Aerospace Science and Engineering  
National University of Defence Technology  
Changsha, Hunan Province 410073, P. R. China  
E-mail: wangshanshan08@nudt.edu.cn

P. Hu, L. Sheng, L. Mao  
National Local Joint Engineering Laboratory for New Petro-chemical Materials and Fine Utilization of Resources  
College of Chemistry and Chemical Engineering  
Hunan Normal University  
Changsha 410081, P. R. China

 The ORCID identification number(s) for the author(s) of this article can be found under <https://doi.org/10.1002/adfm.202210502>.

DOI: 10.1002/adfm.202210502

A. Li, J. Jiang, W. Huang, H. Huang, F. Ouyang  
School of Physics and Electronics  
Central South University  
Changsha 410083, P. R. China

A. Li, F. Ouyang  
School of Physics and Technology  
Xinjiang University  
Urumqi 830046, P. R. China  
E-mail: oyfp@csu.edu.cn

Y. Yu, S. Wang, J. Zhang  
Center for Nanochemistry  
Beijing Science and Engineering Center for Nanocarbons  
Beijing National Laboratory for Molecular Sciences  
College of Chemistry and Molecular Engineering  
Peking University  
Beijing 100871, P. R. China  
E-mail: jinzhang@pku.edu.cn

2D rhenium disulphide (ReS<sub>2</sub>), which belongs to the triclinic system and only consists of an inversion center as the symmetry element, provides an ideal platform.<sup>[14–18]</sup> It adopts two structural characteristics. One is the low in-plane lattice symmetry, which gives rise to significant lateral anisotropy of electrical conductivity, piezoresistance and optics.<sup>[19–21]</sup> The other feature is the weak coupling at the ReS<sub>2</sub>/substrate interface and between ReS<sub>2</sub> layers. It triggers easy deflection of ReS<sub>2</sub> chains during the growth on commonly utilized substrates, which makes the morphology control much more challenging and may lead to disparate mechanisms.<sup>[22–27]</sup> Previous studies have demonstrated that ReS<sub>2</sub> domains grown on mica or sapphire are commonly constructed by the assembly of many subdomains with different orientations.<sup>[25,28]</sup> Only the Au substrate, which has a strong interfacial coupling with ReS<sub>2</sub>, can control the domain shape and lattice alignment of ReS<sub>2</sub> due to the epitaxial growth mechanism.<sup>[29]</sup> On the other hand, the weak interlayer coupling may give more freedom to the stacking configuration and induce novel properties.<sup>[30]</sup> Therefore, investigating the lateral shape and vertical thickness control of 2D ReS<sub>2</sub> can shed light on the morphology engineering and property exploration of a unique class of 2D material that has low in-plane lattice symmetry and weak interlayer coupling.

Herein, we realize the morphology engineering of polycrystalline ReS<sub>2</sub> atomic layers by tailoring the substrate symmetry and the growth temperature using a CVD method. Monolayer ReS<sub>2</sub> exhibits isotropic lateral growth at a low temperature, whereas at a high temperature, the domain shape displays prominent anisotropy that is closely related to the substrate symmetry. Highly oriented square, triangular, and strip-like ReS<sub>2</sub> monolayer polycrystalline domains are achieved on the fourfold symmetry STO (001), threefold symmetry c-sapphire, and twofold symmetry a-sapphire substrates, respectively, which is proposed to be mediated by a diffusion-limited mechanism. The domain thickness reduces monotonically with the growth temperature enhancement, and the electrocatalytic performance exhibits strong thickness dependence. Several interlayer stacking configurations are uncovered in bilayers at the atomic scale. Some are predicted to adopt a type-II band alignment with excellent theoretical power conversion efficiency, showing great potential in photovoltaics.

## 2. Results and Discussion

We developed a double-tube CVD method to grow atomically thin ReS<sub>2</sub> under atmospheric pressure without the addition of hydrogen (H<sub>2</sub>) (Figure S1, Supporting Information), similar to our previously reported approach for the monolayer MoS<sub>2</sub> growth.<sup>[31]</sup> The advantages of such CVD setup include: 1) avoiding the quench of the ReO<sub>3</sub> precursor powder by the upstream S vapor; 2) mitigating the sharp precursor concentration gradient on the substrate compared with the commonly applied face-to-face method (Figures S2 and S3, Supporting Information). The second advantage is especially significant for the following investigation of the morphological engineering since it excludes the potential influence from the growth location of ReS<sub>2</sub> on the substrate. Therefore, the morphological change of the specimen can be solely correlated to our designed

parameters, such as the substrate symmetry and the growth temperature. The thickness and elemental composition of the as-grown monolayer ReS<sub>2</sub> were confirmed by the comprehensive characterizations involving the atomic force microscopy (AFM) (Figure S4, Supporting Information), Raman spectroscopy (Figure S5, Supporting Information), and X-ray photoelectron spectroscopy (XPS) (Figure S6, Supporting Information), respectively.

We first investigated the lateral shape evolution of ReS<sub>2</sub> domains on c-sapphire at different growth temperatures. Figure 1a–c are optical images showing that, as the temperature increased from 700 to 800 °C, the domain shape evolved from circles to arc-sided triangles and finally ended up with well-faceted triangles with sharp edges. The Raman intensity polar plots indicate the polycrystallinity of the as-grown monolayer ReS<sub>2</sub> even for the well-faceted triangular domains because the maximum intensities of the ≈150 cm<sup>-1</sup> peak corresponding to three different locations on the same domain are disparate, situating at ≈75°, ≈100°, and ≈160°, respectively (Figure 1d; Figure S7, Supporting Information). To quantify the shape, change of ReS<sub>2</sub> domains, we introduced a mathematical concept, circularity, which is a measure showing how closely the shape of an object resembles that of a circle. Circularity (*C*) is expressed by:

$$C = \frac{4\pi A}{L^2} \quad (1)$$

where *A* represents the domain area, and *L* is the perimeter length of the domain. The closer *C* is to 1, the more similar the domain is to a perfect circle, indicating significant growth isotropy. In contrast, the closer *C* is to 0, the more anisotropic growth the domain is. Figure 1e statistically presents the circularity distribution of ReS<sub>2</sub> domains synthesized at 700, 750, and 800 °C, respectively. It was achieved by means of a box-counting method (inset of Figure 1e). 100 domains were counted at each temperature. A monotonic decrease of the domain circularity can be clearly seen as the temperature increases. The average circularity of ReS<sub>2</sub> domains is 0.87, 0.76, and 0.65 for the temperature of 700, 750, and 800 °C, respectively. 0.65 is very close to the circularity of an equilateral triangle, which theoretically should be  $\pi/3\sqrt{3}$  (≈0.6). These results quantitatively imply that, as the temperature rises, the polycrystalline ReS<sub>2</sub> domain experiences an isotropic-to-anisotropic growth transition on a single-crystalline c-sapphire substrate. Similar phenomena are also present for ReS<sub>2</sub> grown on a-sapphire and STO (001), where domain shape changes from circle to stripe-like geometry and square, respectively (Figure S8, Supporting Information).

Apart from the shape evolution, the growth temperature enhancement also promotes the alignment of ReS<sub>2</sub> domains. Two preferential orientations twisted by 60° are present, as highlighted by white and red dashed lines in Figure 1c. We quantify these two alignments by measuring the smallest misorientation angle between the ReS<sub>2</sub> domain edge and the [1100] lattice direction of the c-sapphire substrate (inset of Figure 1f). In a collection of 100 domains prepared at temperatures of 750 and 800 °C, respectively, the angle distribution is increasingly concentrated at 0° and 60°, respectively, as the temperature increases (Figure 1e). Similar phenomena have been observed

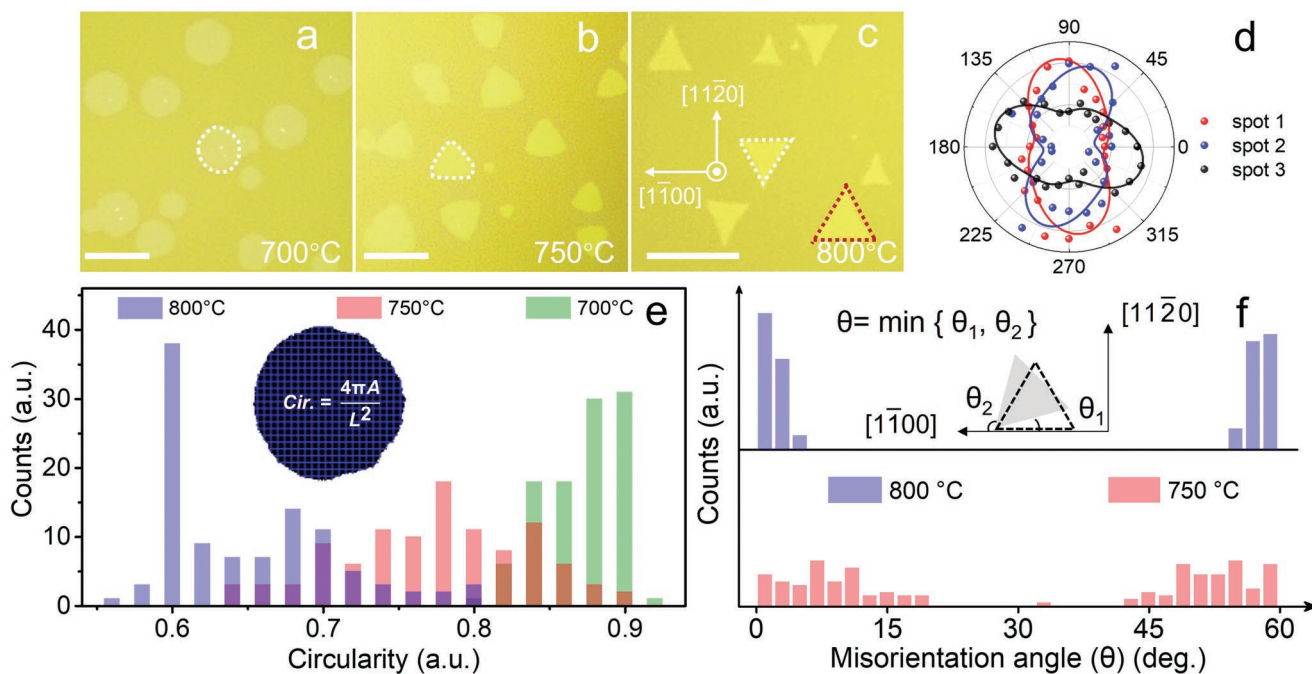


**Figure 1.** a–c) Optical images showing the shape evolution of monolayer ReS<sub>2</sub> grown at 700, 750, and 800 °C, respectively. White and red dashed lines highlight the representative domain profiles at different temperatures. Scale bars: 15 μm. d) Angle-resolved Raman intensities of the vibrational model of monolayer ReS<sub>2</sub> at ≈150 cm<sup>-1</sup> captured at three different locations of a triangular ReS<sub>2</sub> domain grown at 800 °C. e) Histogram displaying the circularity of ReS<sub>2</sub> domains prepared at 700, 750, and 800 °C, respectively. 100 domains were counted at each temperature. f) Histograms showing the statistic orientation distribution of ReS<sub>2</sub> domains grown at 750 and 800 °C, respectively. 100 domains were counted at each temperature.

in high-symmetry 2D materials, but those 2D domains are single crystals.<sup>[32]</sup> Our results indicate the temperature-induced alignment of polycrystalline ReS<sub>2</sub> domains on the single-crystalline substrate. The results indicate the temperature-induced alignment of polycrystalline ReS<sub>2</sub> domains on a single-crystalline c-sapphire substrate (C<sub>3v</sub> symmetry) with a potential correlation between the 2D domain shape and the substrate symmetry at a high growth temperature.

To clarify the above speculation, we grew monolayer ReS<sub>2</sub> on three different substrates at a growth temperature of ≈800 °C. Scanning electron microscopy (SEM) images display that triangular, squared and strip-like ReS<sub>2</sub> domains were grown on c-sapphire, SrTiO<sub>3</sub> (STO) (001) and a-sapphire substrates, respectively, which adopt 3-, 4-, and 2-fold rotational symmetries (Figure 2a–c; Figures S9 and S10, Supporting Information). Figure 2d–f plot the orientation of the ReS<sub>2</sub> domain edges with respect to a specific lattice direction of a substrate. As shown in Figure 2d, the angles between the three domain edges and the [1100] lattice direction of c-sapphire are concentrated at 0°, 60° and 120°, verifying the formation of equilateral triangular domains and matching well with the 3-fold symmetry of the c-sapphire substrate. The angles between the two adjacent domain edges and the [110] lattice direction of STO (001) are concentrated at 0° and 90°, which also shows a good match with symmetry of the substrate (Figure 2e). The long edges of the strip-like domains are well aligned along the [1010] lattice direction of the 2-fold a-sapphire substrate with a narrow orientation distribution at 0°. These results not only indicate the good alignment of ReS<sub>2</sub> domains prepared on various substrates at a high growth temperature, but also verify the

substrate-dependent lateral shape evolution, whose mechanism will be unveiled in Figure 3.

The edge smoothness of a domain is another important in-plane morphological characteristic. Typical SEM images (top insets of Figure 2g) show high edge roughness for flakes on all kinds of substrates, which resemble dendrites. We calculated the fractal dimension of the domain edges by virtue of a standard box-counting approach (Figure S11, Supporting Information). The outline of the flake was extracted followed by filling the outline with squares having a specific pixel size of ε. The number of the squares needed, which is represented by N, has a correlation with the pixel size of the square (ε). The fractal dimension of the flake edge can be achieved by the slope of the linear fitting for the ln(N)-ln(ε) plot (middle insets of Figure 2g). The edge fractal dimensions of domains grown on c-sapphire, STO (001) and a-sapphire are 1.13, 1.14, and 1.24, respectively. All of them are greater than 1, indicating the dendritic morphology of domain edges that deviate from a perfectly smooth line. This feature implies a diffusion-limited growth of ReS<sub>2</sub> domains, which will be discussed in Figure 3.

We performed aberration-corrected annular dark field scanning transmission electron microscopy (ADF-STEM) to conduct the atomic-scale study of ReS<sub>2</sub> domains grown at ≈800 °C, especially grain boundaries (GBs). Figure 2h is a low-magnification ADF-STEM image captured using a scanning moiré fringe (SMF) method.<sup>[33]</sup> It enables to perceive the approximate locations of GBs in a relatively large region (a field of view from tens to hundreds of nanometers), which is time-efficient and lays foundation for the following sub-angstrom-scale imaging. By carefully setting the scanning pixel size to be comparable

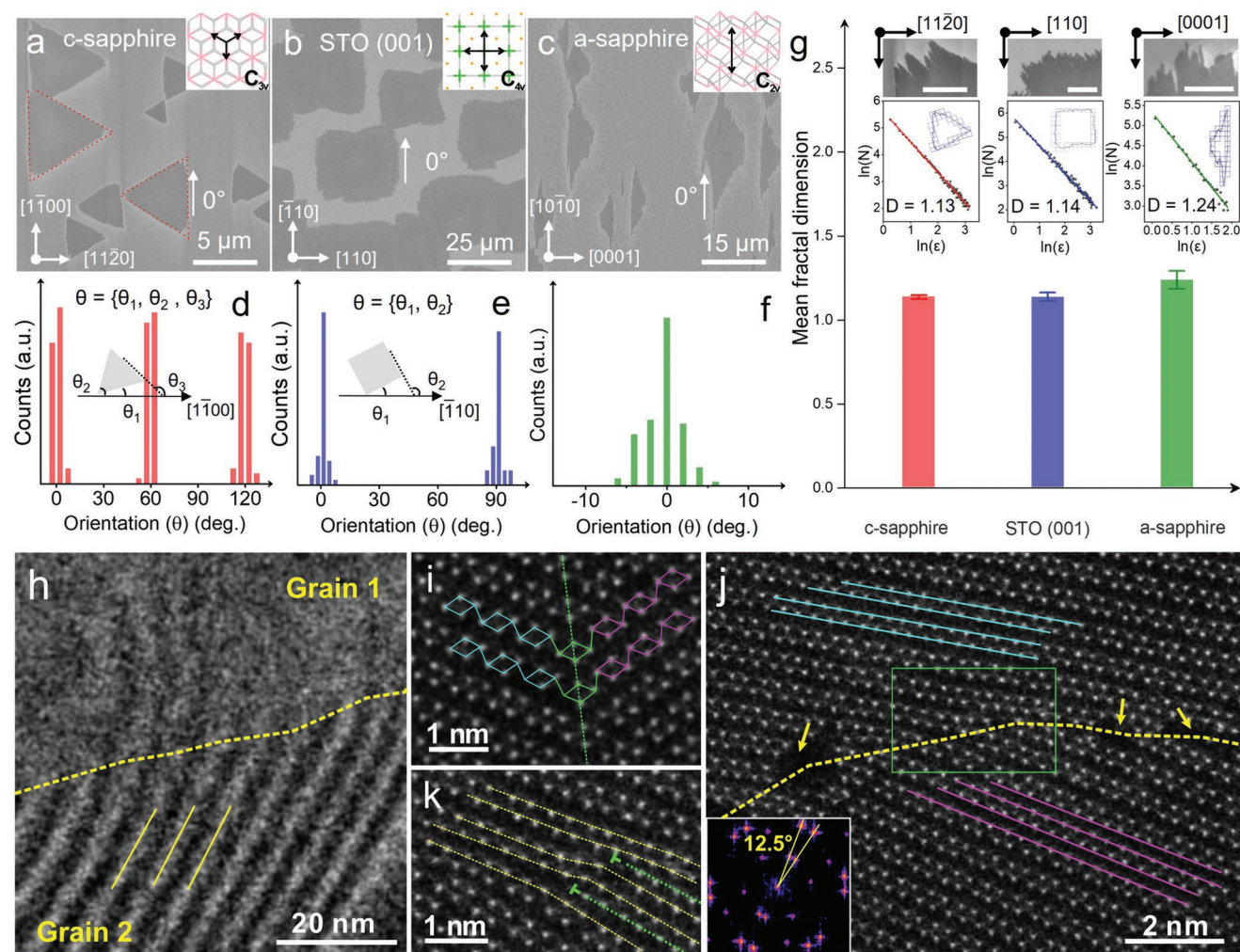


**Figure 2.** a–c) SEM images showing the shape difference of monolayer ReS<sub>2</sub> grown on c-sapphire (C<sub>3v</sub>), STO (001) (C<sub>4v</sub>), and a-sapphire (C<sub>2v</sub>), respectively. Insets provide the lattice models of the three substrates. d–f) Statistics showing the orientation distribution of ReS<sub>2</sub> domains grown on c-sapphire, STO (001), and a-sapphire, respectively. Each substrate counted ≈70 domains. g) Histogram illustrating the fractal dimension of domain edges for ReS<sub>2</sub> grown on c-sapphire, STO (001), and a-sapphire, respectively. Each substrate counted ≈20 domains. Scale bars in SEM images are 1 μm. h) Low-magnification STEM image using the scanning moiré fringes method to show the interface between two grains. Yellow lines show the scanning moiré fringes of Grain 2. The moiré fringes of Grain 1 cannot be displayed in the scope of this image due to a large spacing. i) High-magnification STEM image of a GB with a twist angle of ≈120° between two neighboring grains. Cyan and pink parallelograms represent the Re4 chains in two grains, respectively, while the green parallelograms represent the atomically stitched Re atoms at the GB. j) High-magnification STEM image of a GB with a twist angle of ≈12.5° between the adjacent grains. Cyan and pink lines indicate the directions of the Re4 chains in two grains, respectively. The yellow dashed line highlights the GB. The yellow arrows mark the holes situating at the GB. Inset is the FFT of (j). k) Zoomed-in image of the green-boxed region in (j) showing the atomic configuration of the GB. Two green markers represent the dislocations, while the green dashed lines represent the extra atomic rows along the Re4 chains direction (b axis). The yellow dashed lines are the lattice guide for eyes.

with the lattice spacing of ReS<sub>2</sub>, artificial patterns with disparate moiré fringe spacings were revealed at two sides of a GB (Figure 2h). The yellow dashed line indicates the GB location. We utilized this strategy to identify abundant GBs in ReS<sub>2</sub> domains grown on three types of substrates (Figure S12, Supporting Information). Figure 2i is a zoomed-in ADF-STEM image showing the atomic configuration of the most-frequently observed GBs in our as-grown specimens. The Re4 chains in adjacent grains (labeled by cyan and pink parallelograms) are rotated by ≈120° and atomically stitched with each other at the interface (highlighted by the green parallelograms). Such GBs are energetically favorable as the lattice points of two

grains coincide well with only little distortion at the interface, which has been verified by theoretical calculations in previous reports.<sup>[22,23]</sup> There also exist a small quantity of GBs with arbitrary misorientation angles. Figure 2j displays a typical example, in which two adjoining grains are twisted by ≈12.5°, as certified by the fast Fourier transform (FFT) image of the inset. In stark contrast with the GB shown in panel i, lattice at the interface is severely distorted with holes discretely situated along the GB (pointed by yellow arrows), which may derive from the high chemical reactivity of this type of GB. The zoomed-in view of the green-boxed region in panel j displays two dislocations at a distance of ≈1 nm with symbols of ⊥ at the GB, indicating the

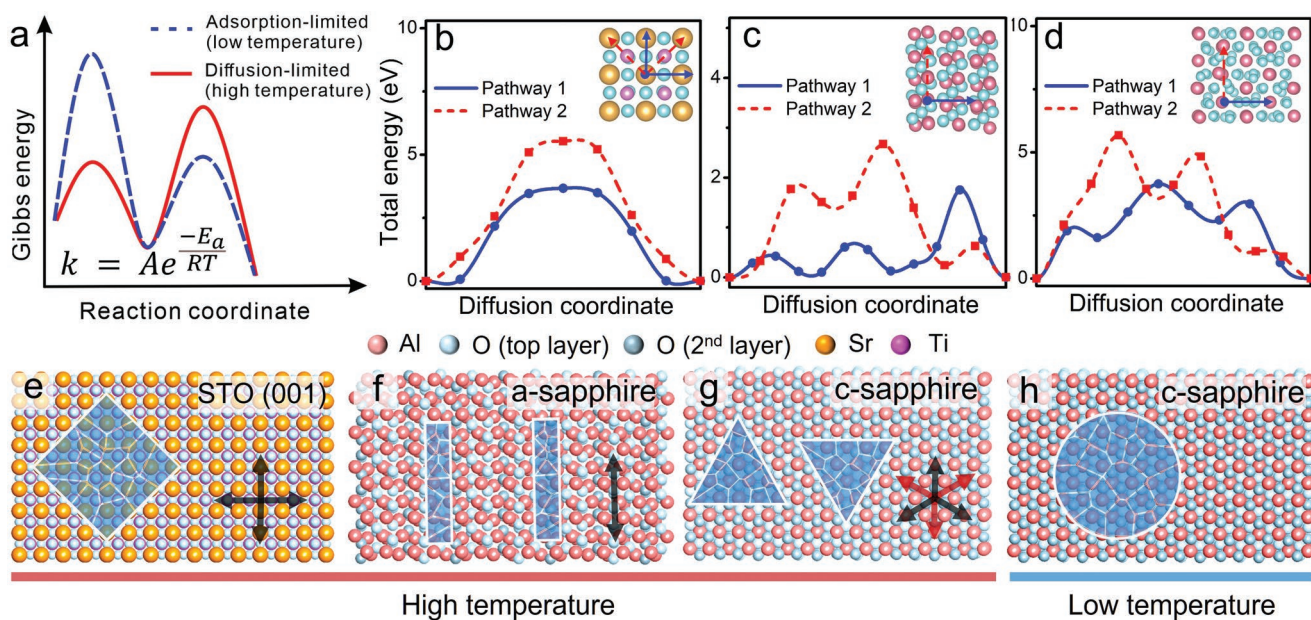


**Figure 3.** a) Schematic energy diagrams for monolayer ReS<sub>2</sub> grown at low temperature and high temperature, respectively. The first peak of the two curves represents the energy barrier of the surface adsorption process of active species on the substrate, while the second peak represents the energy barrier of the surface diffusion process of active species. b–d) DFT-calculated diffusion energy barriers along different paths of the STO (001), a-sapphire and c-sapphire substrate, respectively. The diffusion pathways are represented in insets. e–h) Schematic models illustrating the lateral morphology engineering of ReS<sub>2</sub> domains via substrate symmetry and temperature modulation.

insertion of two extra semi-infinite Re atomic rows along the b axis (Figure 2k). The results verify the polycrystalline nature of ReS<sub>2</sub> domains grown on different substrates at the atomic scale. These domains are generated by intricate patchworks of grains connected by various GBs, consistent with the polarized Raman results in Figure 1d. The polycrystalline domains formed on the single-crystalline substrates may be due to the weak interfacial interaction between ReS<sub>2</sub> and the substrate, as well as a relatively low energy consumption needed for Re<sub>4</sub> chains deflection and reconstruction.<sup>[34]</sup>

We proposed a mechanism to explain two in-plane morphological phenomena observed experimentally: i) at a high growth temperature ( $\approx 800$  °C), the shape of the polycrystalline domains shows a correlation with the substrate rotational symmetry, and the domains are well oriented on the single crystalline substrates (Figure 2); ii) at a low growth temperature ( $\approx 700$  °C), the polycrystalline ReS<sub>2</sub> domains experience anisotropic-to-isotropic growth transition (Figure 1). In brief, the first phenomenon is attributed to a diffusion-limited growth at a high temperature (red curve in Figure 3a). The diffusion anisotropy of precursors on the substrate is strongly dependent on the substrate symmetry. The second phenomenon is ascribed to the synergistic effect of both an adsorption-limited growth at the low temperature (blue dashed curve in Figure 3a) and the polycrystalline structure of the ReS<sub>2</sub> domains.

Density functional theory (DFT) calculations were first conducted to identify the preferential diffusion directions of Re atoms on three different substrates. This is because S vapor is in excess during the synthesis. Therefore, the supply of Re atoms determines the growth of ReS<sub>2</sub> domains. Taking the 4-fold STO (001) substrate as an example (Figure 3b), the blue and red curves display the diffusion energy barriers of Re

atoms along the Sr-O-Sr direction (blue arrows, [100] direction, Pathway 1) and the Sr-Ti-Sr direction (red arrows, [110] direction, Pathway 2), respectively. It shows that the diffusion energy barrier along Pathway 1 is only 3.7 eV, which is profoundly smaller than that along Pathway 2, which is 5.5 eV. The remarkable energy difference stems from the Coulomb interaction between precursor active species and the surface ions. Our DFT calculations show that the center of the four nearest oxygen atoms is the most stable adsorption site for Re atoms. Mulliken's population analysis suggests that each Re atom transfers about one electron to the substrate and forms the Re<sup>+</sup> ion. The diffusion energy in Figure 3b reaches the saddle point when the Re<sup>+</sup> ion is on the top of the O<sup>2-</sup> for Pathway 1 (Sr-O-Sr). For Pathway 2 (Sr-Ti-Sr), the saddle point corresponds to the transition structure of the Re<sup>+</sup> ion directly above the Ti<sup>4+</sup> ion. We infer that the strong Coulomb attraction between the Re<sup>+</sup> ion and the neighboring O<sup>2-</sup> ions contribute to the reduction of the diffusion barrier for Pathway 1. In contrast, the Coulomb repulsion between Re<sup>+</sup> and Ti<sup>4+</sup> improves the barrier for Pathway 2, thus making the diffusion along Sr-Ti-Sr to be energetically inferior to that along Sr-O-Sr. Therefore, when the preparation of ReS<sub>2</sub> is controlled by the diffusion step, the growth rate of ReS<sub>2</sub> along Pathway 1 is faster than that along Pathway 2. Due to the 4-fold lattice symmetry of STO (001), the angle between two blue arrows corresponding to Pathway 1 is 90°. So do the two red arrows for Pathway 2. Therefore, the domain shape of ReS<sub>2</sub> grown on the 4-fold STO (001) is square (Figure 3e). The diagonal directions of the square (black arrows in Figure 3e), which are the fastest growth orientations, are parallel with the preferential diffusion directions of precursors (Pathway 1). Moreover, since the substrate is single crystalline, the preferential diffusion directions at different regions are oriented in

the same direction, thus leading to the formation of aligned ReS<sub>2</sub> domains across the substrate. It is worth noting that many well-aligned 2D material formation reported previously are derived from the epitaxial growth of the single crystalline 2D domains on the substrate.<sup>[35]</sup> However, in our experiment, both polarized Raman spectroscopy and ADF-STEM have proved the polycrystalline structure of the ReS<sub>2</sub> domains. Hence, the epitaxial growth mechanism that results in the uniform domain alignment can be excluded. In addition, the diffusion-limited growth commonly leads to rough domain edges and dendritic morphology,<sup>[35,36]</sup> agreeing with our observations in Figure 2g. The compactness of a domain grown in the diffusion-limited regime is controlled by the diffusion ability of adatoms along domain edges (in other words, the relaxation extent of adatoms after attaching to domain edges).<sup>[37]</sup> The more sufficient the edge relaxation is, the higher the domain compactness will be. Based on our results, the edge diffusion of adatoms on the ReS<sub>2</sub> domains in our growth condition is inferred to be sufficient, thus leading to a relatively high overall domain compactness with dendritic features mainly revealed at rugged edges.

The strip-like domains formed on the a-sapphire substrate can be understood in a similar way. DFT calculations show that diffusion along the [10 $\bar{1}$ 0] direction (blue arrow) is energetically favorable with an energy barrier of 1.8 eV (Figure 3c). Since the lattice symmetry of a-sapphire is 2-fold, which means it appears identical after a rotation of 180°, the ReS<sub>2</sub> domains grown on a-sapphire adopt ribbon-like geometry, which extend along the lattice direction of [10 $\bar{1}$ 0] of a-sapphire (black arrows in Figure 3f). For the c-sapphire substrate (Figure 3d), the diffusion energy barrier along the [11 $\bar{2}$ 0] direction (blue arrow, Pathway 1) is only 3.7 eV, which is 1.1 eV lower than that along the [1 $\bar{1}$ 00] direction (red arrow, Pathway 2). Since c-sapphire adopts 3-fold symmetry, the as-grown ReS<sub>2</sub> display two groups of equilateral triangles with a twist angle of 60° to each other (Figure 3g). The directions of the lines connecting the center of the equilateral triangles and the vertices, which are the fastest growth orientations, are parallel to Pathway 1 (represented by black and red arrows, Figure S13, Supporting Information). The reason why ReS<sub>2</sub> domains on c-sapphire are triangles rather than hexagons may arise from the two sets of degenerated edge structures along the six equivalent directions of <11 $\bar{2}$ 0> for the 3-fold c-sapphire,<sup>[38]</sup> the defect-influenced nucleation at the initial stage,<sup>[39]</sup> and the detailed growth conditions.

When the growth temperature is decreased, the ReS<sub>2</sub> domain shape evolves to an isotropic circle (Figure 3h). It is ascribed to the potential change of the rate-limiting step, altering from the diffusion-limited growth, which is highly dependent on the substrate lattice directions, to the adsorption-limited growth that is orientation-independent (blue dashed curves in Figure 3a). In this scenario, the domain shape is not determined by the diffusion rate discrepancy of the precursor molecules along different lattice directions on the substrate, thus losing correlation with the substrate symmetry. Moreover, since the Re<sub>4</sub> chains are prone to deflect during the ReS<sub>2</sub> growth, the macroscopic shape of the domains also does not show a correlation with the intrinsic configuration of the triclinic ReS<sub>2</sub> single crystal, in which the extension along b axis is energetically favorable.<sup>[40]</sup> Therefore, the polycrystalline configuration of ReS<sub>2</sub> domains

brings about an average growth rate in all directions, leading to the formation of round flakes.

We then studied the vertical morphology of ReS<sub>2</sub>, including the thickness control and the atomic-scale stacking configurations. In order to make the phenomenon more obvious, the vapor concentration of ReO<sub>3</sub> was slightly increased. Under this condition, the domain thickness reduced as the growth temperature enhanced from 700 to 800 °C (Figure 4a–c; Figure S14, Supporting Information). To investigate the domain thickness uniformity across a large region, we developed an approach to evaluate the monolayer rate of ReS<sub>2</sub> (the ratio of the monolayer area to the total area of the 2D product) by means of the optical contrast. First, the optical contrast of a typical monolayer region, whose thickness has been confirmed by AFM, was calibrated. Then, a software was applied to perform peak fitting on the total contrast distribution curve of a substrate that involves ReS<sub>2</sub> with different thickness in an optical image. The monolayer rate of the product across a large region can be figured out by calculating the area ratio of the peak corresponding to the monolayer contrast to the peaks corresponding to the total product contrast (Figure S15, Supporting Information). The results show that the monolayer rate increases as the growth temperature rises (Figure 4e), yielding a ratio of ≈99% at ≈800 °C. It may stem from the promotion of the precursor diffusion ability on the substrate surface as the temperature enhances, thus facilitating the Frank-van der Merwe growth.

The atomic-scale stacking configurations of few-layer ReS<sub>2</sub> were then unveiled. Figure 4d is a low-magnification ADF-STEM image, in which the intensity line profile taken along the yellow dashed line indicates that mono-, bi- and trilayer are involved in this region. The secondary layers of ReS<sub>2</sub> grown on the monolayer exhibit long branches (cyan arrows), which extend along the b axis by a zoomed-in view (Figure S16, Supporting Information). This phenomenon is consistent with the low formation energy of ReS<sub>2</sub> edges along the b axis. The atomic registries at bilayer regions are investigated by high-magnification ADF-STEM imaging. Interestingly, distinct from the high-symmetry 2D materials (e.g., graphene and 2H-MoS<sub>2</sub>), which exhibit only a few interlayer stacking configurations,<sup>[41]</sup> bilayer ReS<sub>2</sub> shows a rich diversity of interlayer stacking. Figure 4f,i and l display three typical moiré patterns at bilayer regions. The Re<sub>4</sub> chain directions (b axis) of two layers are parallel to each other for all three examples, but the alignment of atoms in the upper and lower layers are flexible. Moreover, the orientations of the Re parallelograms are the same in panels f and i, while the Re parallelograms in the top layer in panel l is turned over compared with those in the bottom layer. We deduced the atomic models (Figure 4g,j,m) and conducted image simulation (Figure 4h,k,n), which match well with the experimental images. It is worth noting that, due to the large atomic number difference between the Re and S element, ADF-STEM can only observe Re atoms with S atoms invisible. Therefore, for each stacking configuration of Re<sub>4</sub> chains shown in Figure 4g,j, and m, there exist two potential atomic models if taking the position of S atoms into account (Figure S17, Supporting Information). DFT calculations were performed to unveil the total energies of bilayer ReS<sub>2</sub> corresponding to these six different interlayer atomic registries. Only subtle energy difference of less than 0.8 meV/ReS<sub>2</sub> is shown (Figure S17, Supporting Infor-

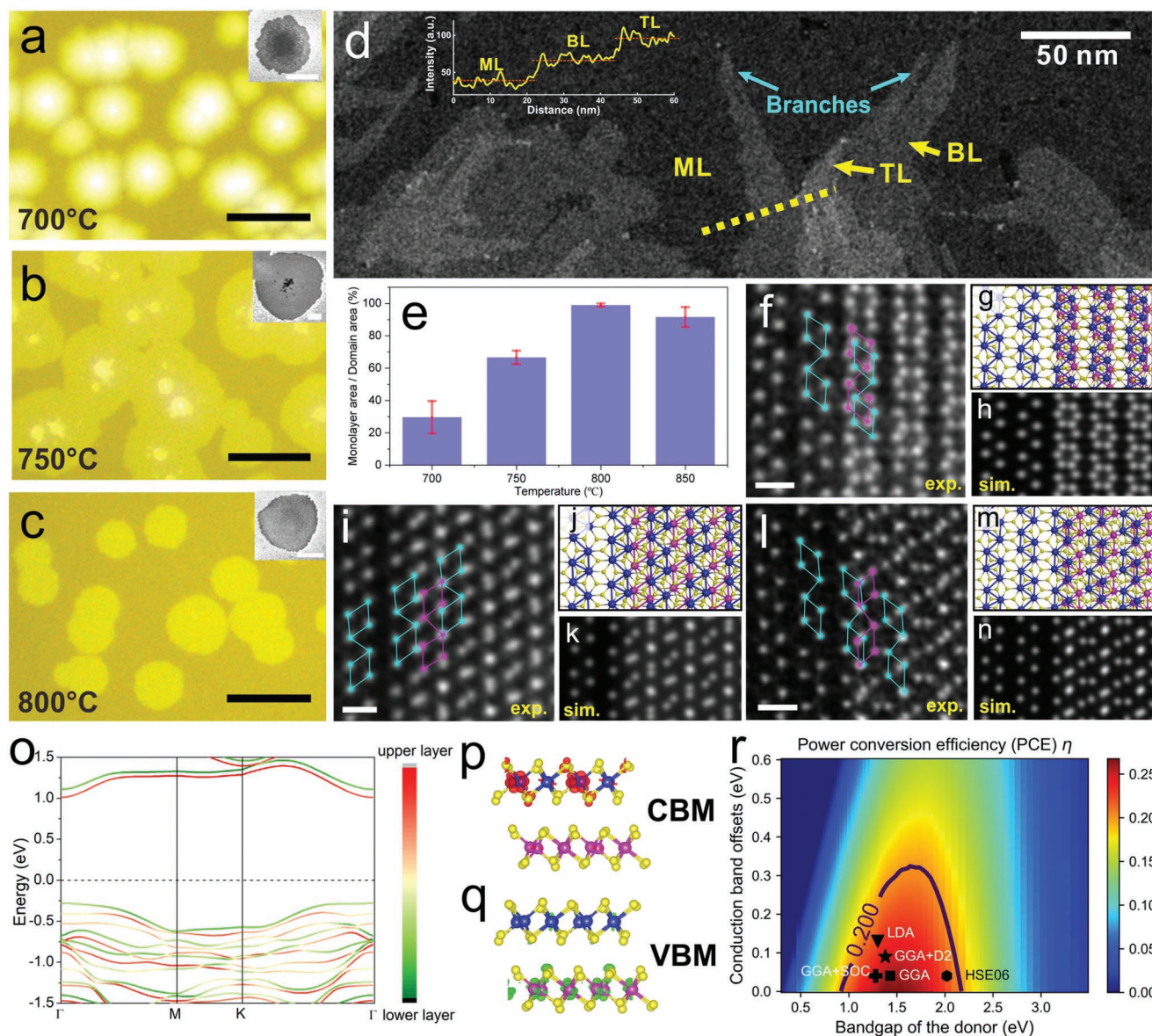


**Figure 4.** a–c) Optical images showing the thickness evolution of ReS<sub>2</sub> domains synthesized at 700, 750, and 800 °C, respectively, under an increased ReO<sub>3</sub> vapor concentration. Scale bars: 20 μm. Insets are SEM images. Scale bars: 5 μm. d) Low-magnification STEM images of a multilayer ReS<sub>2</sub> region. ML, BL and TL represent monolayer, bilayer and trilayer ReS<sub>2</sub> areas, respectively. The top inset shows the intensity line profile along the yellow dashed line. e) Histogram showing the monolayer rate (the ratio between the monolayer area and the domain total area) for ReS<sub>2</sub> prepared at different temperatures. f, i, l) High-magnification STEM images of three types of typical atomic registries in bilayer ReS<sub>2</sub>. Scale bars: 0.5 nm. g, j, m) Atomic models corresponding to the ADF-STEM images in (f), (i) and (l), respectively. h, k, n) Simulated images based on the models in (g), (j) and (m), respectively. o) The layer-resolved projected band structure of asymmetrically stacking bilayer ReS<sub>2</sub> calculated by the DFT+D2 method. p, q) visualized CBM (p) and VBM (q) for bilayer ReS<sub>2</sub> with the contour surface set as 10<sup>-4</sup> Å<sup>-3</sup>. r) Power conversion efficiency (PCE) for the asymmetrically stacking bilayer ReS<sub>2</sub>.

mation). Stack-1A, Stack-2B, and Stack-3A are the most energetically favorable, which suggest the most potential interlayer stacking configurations corresponding to the experimental images of Figure 4f, i, and l, respectively. These results unfold the polymorphism of bilayer ReS<sub>2</sub>, which only requires the parallelism of the Re<sub>4</sub> chains directions in two layers without strict restrictions on the alignment of atoms between layers. It may originate from the weak interlayer coupling of low-symmetry ReS<sub>2</sub> due to Peierls distortion<sup>[22]</sup> that leads to only slight energy variation between different interlayer stackings.

Interestingly, some stacking configurations can break the inversion symmetry and induce spontaneous vertical electric polarization in bilayer ReS<sub>2</sub>. Take Stack-2B corresponding to Figure 4i as an example, the layer-resolved projected band structure is displayed in Figure 4o, in which the band degeneracy between two layers is removed due to inversion symmetry breaking, leading to a band offset of 0.1 eV (Figures S18 and S19, Supporting Information). As displayed in Figure 4p and q, the conduction band minimum (CBM) is localized in the upper layer of ReS<sub>2</sub>, while the valance band maximum (VBM)



is mainly contributed by the lower layer, suggesting a type-II band alignment. Further DFT calculations suggest that the vertical dipole moment of the bilayer is only  $3.8 \times 10^{-3} e \text{ \AA}$  per unit cell, which cannot induce such a perceptible band offset in Figure 4o. Therefore, the type-II band alignment in bilayer  $\text{ReS}_2$  should be directly caused by the asymmetric interface instead of the interlayer charge transfer.

The type-II bands alignment and 1.4 eV direct bandgap make bilayer  $\text{ReS}_2$  a promising candidate for photovoltaics. Power conversion efficiency (PCE) is the most important quality of heterojunction solar cells. For heterostructures, PCE can be estimated from DFT results by:<sup>[42]</sup>

$$\eta = \frac{0.65(E_g - \Delta E_C - 0.3) \int_{E_g}^{\infty} \frac{P(\hbar\omega)}{\hbar\omega} d\hbar\omega}{\int_0^{\infty} P(\hbar\omega) d\hbar\omega} \quad (2)$$

where  $E_g$  is the bandgap of the donor,  $\Delta E_C$  is the conduction band offsets, and  $P(\hbar\omega)$  represents the Air Mass 1.5 (AM1.5) solar energy flux. Figure 4r displays PCE as a function of  $E_g$  and  $\Delta E_C$  corresponding to the Stack-2B interlayer registry, in which the positions of the bilayer  $\text{ReS}_2$  performance are marked by points. Although the bandgaps obtained from different DFT methods vary from 1.2 to 2.0 eV, the PCE of bilayer  $\text{ReS}_2$  is always higher than 20%, which is competitive with other types of 2D heterojunctions.<sup>[43,44]</sup> Since the bilayer  $\text{ReS}_2$  with inversion symmetry breaking has a high PCE and can be seen as

a natural p-n homojunction without foreign atom doping or electrical gating, it may show great potential in high-efficiency photoelectric applications.

We finally investigated the vertical morphology influence on the material property by measuring the electrocatalytic hydrogen evolution reaction (HER) performance of  $\text{ReS}_2$  with different thickness. The HER activities of monolayer and multilayer  $\text{ReS}_2$  were characterized using a typical three-electrode setup in 0.5 M  $\text{H}_2\text{SO}_4$  solution (Figures S20–S22, Supporting Information). The polarization curve ( $i$ - $V$  plot) shows that the onset potential of monolayer  $\text{ReS}_2$  is 273 mV at the current density of  $3 \text{ mA cm}^{-2}$ , which is  $\approx 130 \text{ mV}$  lower than that of the multilayer counterparts (Figure 5a). The catalytic performance remained stable for monolayer  $\text{ReS}_2$  after 3000 cycles (inset of Figure 5a). By fitting the linear portion of the Tafel plots to the equation of  $\eta = a + b \log j$  (overpotential  $\eta$ , Tafel slope  $b$ , current density  $j$ ), we figured out Tafel slopes of 100 mV/decade and 142 mV/decade for monolayer and multilayer  $\text{ReS}_2$ , respectively, indicating inferior reaction kinetics of multilayers (Figure 5b). The Tafel slope of pristine monolayer  $\text{ReS}_2$  measured in our experiment is superior to some previous reports.<sup>[45,46]</sup> It could be induced by both the atomic thinness and the abundant GBs in the specimen, among that some defective structures may facilitate the improvement of electrocatalytic properties.

The thickness-dependent catalytic properties can be attributed to the vertical conductivity discrepancy between monolayer and multilayer  $\text{ReS}_2$ . It has been reported that the interlayer resistivity of  $\text{ReS}_2$  ( $\approx 10^5 \Omega \mu\text{m}$ ) is approximately two orders of

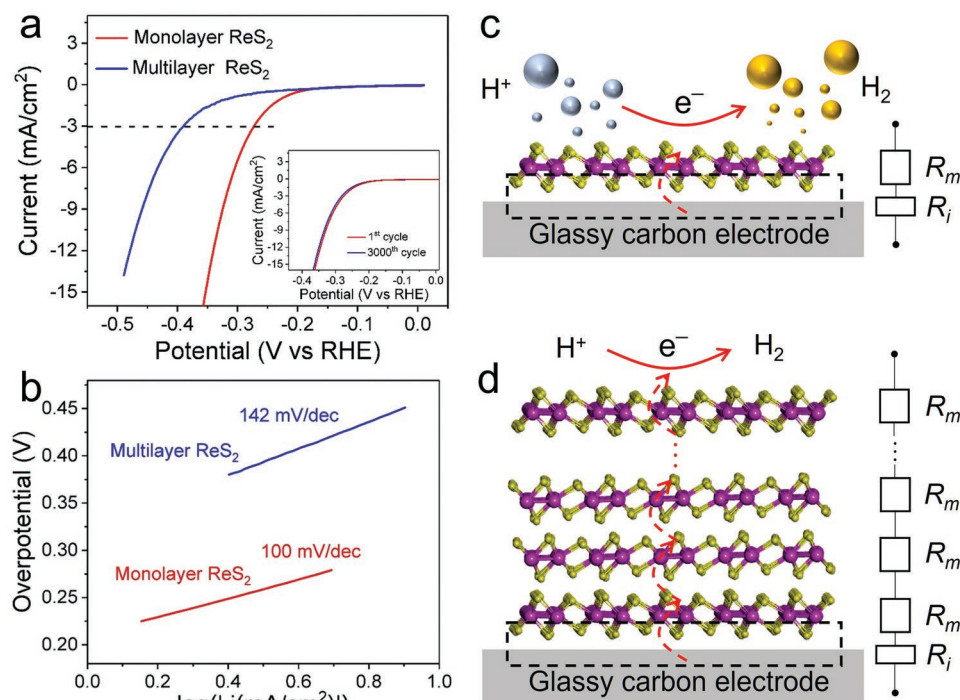


**Figure 5.** a) Polarization curves for monolayer (red) and multilayer (blue)  $\text{ReS}_2$  films, respectively. Inset is the long stability test comparing the polarization curves between the 1st cycle and the 3000th cycle for monolayer samples. b) Tafel plots corresponding to the results in (a). c,d) Schematics demonstrating the mechanism behind different electrocatalytic performance of monolayer and multilayer  $\text{ReS}_2$ . The dashed red arrows indicate the interlayer hopping of electrons. The  $\text{ReS}_2$  resistance between each two layers and the  $\text{ReS}_2$ /substrate interfacial resistance are represented by  $R_m$  and  $R_i$ , respectively.

magnitude greater than those of other 2D TMDs, such as MoS<sub>2</sub> ( $\approx 10^3 \Omega \mu\text{m}$ ) due to Peierls distortion-induced weak interlayer coupling in ReS<sub>2</sub>.<sup>[47]</sup> Such large interlayer resistivity decreases the number of accessible active sites on the outermost ReS<sub>2</sub> layer that directly contact with the electrolyte. This is because electrons from the electrode need to hop vertically layer by layer until reaching the top layer to participate in the electrocatalytic reaction at active sites. Hopping through each layer must overcome an interlayer potential barrier that will reduce the number of electrons. Therefore, the thicker the sample is, the less quantity of electrons can reach the outermost layer for HER reaction, thus leading to higher overpotentials (left panels in Figure 5c,d). Similar phenomena have also been observed in multilayer MoS<sub>2</sub> and should be more remarkable in ReS<sub>2</sub> with an increased interlayer resistance.<sup>[48]</sup>

It is noteworthy that the HER performance difference between monolayer and multilayer ReS<sub>2</sub> domains in our experiment is not due to edges, even though they commonly contribute a lot to the overall electrochemical performance of 2D materials, especially for vertically grown 2D nanosheets, 3D nanoflowers, and monolayer dendritic domains.<sup>[49–51]</sup> This is because Figure 5a and b show that monolayer ReS<sub>2</sub> exhibits a better catalytic performance than multilayers. If we attribute such phenomenon to the difference in edges, since multilayer ReS<sub>2</sub> adopts more edges than monolayers, multilayer ReS<sub>2</sub> should perform better in electrochemistry than the monolayer counterparts, which is just the opposite to the experimental results. Therefore, the possibility that the thickness-dependent catalytic performance is due to edges can be ruled out. Someone may argue that, even though multilayer ReS<sub>2</sub> have more edges than monolayers, the edge structures in monolayer and multilayer ReS<sub>2</sub> could be different. If the edge structure in monolayers has a higher catalytic activity than multilayers, it is still possible that better electrochemical performance in monolayers is due to edges. We conducted ADF-STEM experiments and uncovered that the edge configurations of mono- and multilayer ReS<sub>2</sub> are the same at the atomic scale (Figure S23, Supporting Information), which excludes the above hypothesis. The reason why edges do not dominate the HER property in atomically thin 2D ReS<sub>2</sub> could stem from the spatial decoupling of the edges sites in the laterally grown multilayer ReS<sub>2</sub> from the GC electrode and a high interlayer potential barrier in this type of weakly coupled van der Waals material that makes the electron hopping between layers become the dominant factor for the electrocatalytic property.<sup>[52]</sup>

The increase of the Tafel slope for multilayer ReS<sub>2</sub> compared with the monolayer counterparts can also be attributed to the large interlayer resistivity that results in a prominent ohmic resistance between the electrode and the outermost ReS<sub>2</sub> layer. Previous work addressed that the Tafel slope is influenced by both the intrinsic properties of the material and the ohmic resistance of the electrode, as expressed by the following equation:

$$\frac{d\eta}{d\ln i} = b + \frac{R_i}{3} \quad (3)$$

where  $d\eta/d\ln i$  represents the measured Tafel slope experimentally,  $b$  represents the intrinsic Tafel slope of the material,

and  $R$  represents the ohmic resistance between the electrode and the catalytic material.<sup>[53,54]</sup> If abstracting the ReS<sub>2</sub> resistance between each two layers and the ReS<sub>2</sub>-substrate interfacial resistance as  $R_m$  and  $R_i$ , respectively, the ohmic resistance between the active sites (in the top layer) and the electrode for multilayer ReS<sub>2</sub> is clearly larger than that for monolayers, which results in a larger measured Tafel slope (right panels in Figure 5c,d). In other words, the real potential that active sites in a multilayer sample can “feel” is severely smaller than those in the monolayer counterparts, thus deteriorating the kinetic parameter of Tafel slope. These results demonstrate the importance of thickness control for the catalytic performance optimization of ReS<sub>2</sub>.

### 3. Conclusion

To sum up, with a combination of experimental characterizations and theoretical calculations, we unraveled the lateral growth behavior of polycrystalline monolayer ReS<sub>2</sub>, which is isotropic at a low growth temperature but displays substrate-symmetry dependent anisotropy with orientational uniformity of 2D domains at a high growth temperature due to a diffusion-limited mechanism. Such growth mechanism is considered to be in stark difference from those of epitaxially grown single-crystalline 2D flakes predominantly driven by either favorable adsorption energy at the 2D material-substrate interface or the superior binding energy between 2D material edges and the substrate steps. The thickness of ReS<sub>2</sub> also shows great dependence on the growth temperature and can influence the HER performance. Various stacking configurations in bilayer ReS<sub>2</sub> are uncovered, which restrict the orientation of Re4 chains in different layers but give high flexibility to registry of interlayer atoms. This is in stark contrast to most high-symmetry bilayer 2D counterparts with limited interlayer coupling modes (e.g., graphene and 2H-MoS<sub>2</sub>) and provides some special stacking structures with broken inversion symmetry that adopt a type-II band alignment with high theoretical power conversion efficiency. This work demonstrates feasibility and mechanism of engineering the lateral shape and the vertical thickness of a special class of 2D material (low in-plane lattice symmetry and weak interlayer coupling) polycrystalline domains by tailoring substrate symmetry and the growth temperature. It enriches the comprehension of the morphology control of 2D materials that is crucial for their high-quality synthesis and industrial applications.

### 4. Experimental Section

**Growth and Transfer of 2D ReS<sub>2</sub>:** 2D ReS<sub>2</sub> was grown by a hydrogen-free atmospheric pressure chemical vapor deposition (APCVD) method with rhenium trioxide (ReO<sub>3</sub>, 99.9%, Sigma-Aldrich, 2 mg) and sulphur (S, 99.5%, Sigma-Aldrich, 200 mg) powder used as precursors. C-sapphire, STO (001), a-sapphire, and Si/SiO<sub>2</sub> can be used as the substrate. The crucible containing ReO<sub>3</sub> was located at the furnace center, maintaining temperature of 700 – 850 °C for the ReS<sub>2</sub> growth, while S powder was placed upstream of the furnace with heating temperature of  $\approx 200$  °C. The reaction lasted for 15 min. The furnace was naturally cooled to room temperature after growth. For the transfer of 2D ReS<sub>2</sub>, a thin film

of poly (methyl methacrylate) (PMMA) was initially spin-coated on the ReS<sub>2</sub>/substrate surface. Subsequently, the sample was gently floated on a 2 mol L<sup>-1</sup> potassium hydroxide (KOH) solution. When the PMMA/ReS<sub>2</sub> film detached from the substrate, the film was transferred to the deionized water for three times to thoroughly remove residuals left by the etchant. The film was then transferred to a TEM grid or a glass carbon rod, dried naturally in the air and baked on the hotplate at 180 °C for 15 min. The PMMA scaffold was finally removed by submerging the TEM grid in acetone for 8 h.

**Scanning Transmission Electron Microscopy and Image Processing:** ADF-STEM imaging was conducted at room temperature on an aberration-corrected Titan Cubed Themis G2 300. STEM was operated under an accelerating voltage of 300 kV. Conditions were a condenser lens aperture of 50 mm, convergence semi-angle of 21.3 mrad, and collection angle of 39–200 mrad. Dwell time of a single frame was 2 μs per pixel. A pixel size of 0.012 nm px<sup>-1</sup> as well as a beam current of 30 pA was used for imaging. Images were processed using the ImageJ software. A Gaussian blur filter (≈2–4 pixels) was used on high-magnification ADF-STEM images for smoothing. A fire or orange hot false color LUT was applied to some grayscale ADF-STEM images to improve the visualization. Atomic models were constructed using the software of Accelrys Discovery Studio Visualizer. ADF-STEM image simulations based on corresponding atomic models were generated using COMPUTEM software with a proper parameter adjustment in light of the imaging conditions.

**Calculation Methods:** All DFT calculations used exchange correlation potential described by the generalized gradient approximation (GGA) in the PBE functional unless otherwise specified. The diffusion energy barriers were calculated using the nudged elastic band (NEB) method, which were implemented in the QuantumATK package with a linear combination of basis sets of atomic orbitals (LCAO).<sup>[55]</sup> The bilayer ReS<sub>2</sub> calculations were implemented in the Vienna Ab-initio Simulation Package (VASP)<sup>[56]</sup> and used the projector augmented wave (PAW) method<sup>[57]</sup> to treat the core electrons. The force convergence criterion was set to 0.01 eV Å<sup>-1</sup> for the structural optimization of bilayer ReS<sub>2</sub> and was reduced to 0.1 eV Å<sup>-1</sup> in the NEB calculations. In PCE calculations, for comparison, it had also performed standard DFT calculations based on local density approximation (LDA), and GGA calculations considering van der Waals (vdW) correction in the DFT-D2 method<sup>[58]</sup> (GGA+D2), GGA calculations considering spin-orbit coupling effects (GGA+SOC), and hybrid functional calculations in the HSE06 method.

## Supporting Information

Supporting Information is available from the Wiley Online Library or from the author.

## Acknowledgements

S.W. acknowledges support from the National Natural Science Foundation of China (52172032, 52222201), Young Elite Scientist Sponsorship Program by CAST (YESS20200222), State Administration of Science, Technology, and Industry for National Defense (WDZC20195500503), National University of Defense Technology (ZK18-01-03), and Hunan Natural Science Foundation (2022JJ20044). J.Z. acknowledges financial support from the Ministry of Science and Technology of China (2016YFA0200100 and 2018YFA0703502), the National Natural Science Foundation of China (Grant Nos. 52021006, 51720105003, 21790052, 21974004), the Strategic Priority Research Program of CAS (XDB36030100), and the Beijing National Laboratory for Molecular Sciences (BNLMS-CXTD-202001). This work was carried out in part using computing resources at the High Performance Computing Center of Central South University. O.F. acknowledges the National Natural Science Foundation of China (Grant No. 52073308).

## Conflict of Interest

The authors declare no conflict of interest.

## Author Contributions

H.P., H.Z., A.L., and L.S. contributed equally to this work. J.Z. and S.W. initiated the project and generated the experimental protocols. P.H., H.Z., and L.S. conducted CVD experiments. A.L. and F.O. performed DFT calculations. Y.Y. and S.W. fabricated the STEM sample and conducted ADF-STEM imaging. All authors contributed to the data analysis, manuscript writing and revision of the manuscript.

## Data Availability Statement

The data that support the findings of this study are available from the corresponding author upon reasonable request.

## Keywords

2D, ADF-STEM, chemical vapor deposition, low symmetry, morphology engineering, ReS<sub>2</sub>, weakly coupled

Received: September 9, 2022

Revised: November 6, 2022

Published online:

- [1] X. Sang, X. Li, W. Zhao, J. Dong, C. M. Rouleau, D. B. Geohegan, F. Ding, K. Xiao, R. R. Unocic, *Nat. Commun.* **2018**, *10*, 1038.
- [2] W. Xu, S. Li, S. Zhou, J. K. Lee, S. Wang, S. G. Sarwat, X. Wang, H. Bhaskaran, M. Pasta, J. H. Warner, *ACS Appl. Mater. Interfaces* **2018**, *10*, 4630.
- [3] M. Hassan, E. Haque, K. R. Reddy, A. I. Minett, J. Chen, V. G. Gomes, *Nanoscale* **2014**, *6*, 11988.
- [4] G. Z. Magda, X. Jin, I. Hagymási, P. Vancsó, Z. Osváth, P. Nemes-Incze, C. Hwang, L. P. Biró, L. Tapasztó, *Nature* **2014**, *514*, 608.
- [5] K. F. Mak, C. Lee, J. Hone, J. Shan, T. F. Heinz, *Phys. Rev. Lett.* **2010**, *105*, 136805.
- [6] Y. Cao, V. Fatemi, S. Fang, K. Watanabe, T. Taniguchi, E. Kaxiras, P. Jarillo-Herrero, *Nature* **2018**, *556*, 43.
- [7] K. Yasuda, X. Wang, K. Watanabe, T. Taniguchi, P. Jarillo-Herrero, *Science* **2021**, *372*, 1458.
- [8] O. Hod, E. Meyer, Q. Zheng, M. Urbakh, *Nature* **2018**, *563*, 485.
- [9] S. Wang, Y. Rong, Y. Fan, M. Pacios, H. Bhaskaran, K. He, J. H. Warner, *Chem. Mater.* **2014**, *26*, 6371.
- [10] Z. Ma, S. Wang, Q. Deng, Z. Hou, X. Zhou, X. Li, F. Cui, H. Si, T. Zhai, H. Xu, *Small* **2020**, *16*, 2000596.
- [11] Y. Zhang, Q. Ji, J. Wen, J. Li, C. Li, J. Shi, X. Zhou, K. Shi, *Adv. Funct. Mater.* **2016**, *26*, 3299.
- [12] F. Cui, X. Zhao, J. Xu, B. Tang, Q. Shang, J. Shi, Y. Huan, J. Liao, Q. Chen, Y. Hou, Q. Zhang, S. J. Pennycook, Y. Zhang, *Adv. Mater.* **2020**, *32*, 1905896.
- [13] Z. Cai, B. Liu, X. Zou, H. M. Cheng, *Chem. Rev.* **2018**, *118*, 6091.
- [14] X. He, F. Liu, P. Hu, W. Fu, X. Wang, Q. Zeng, W. Zhao, Z. Liu, *Small* **2015**, *11*, 5423.
- [15] M. Hafeez, L. Gan, H. Li, Y. Ma, T. Zhai, *Adv. Funct. Mater.* **2016**, *26*, 4551.
- [16] P. Chen, J. Wang, Y. Lu, S. Zhang, Z. Wang, L. Wang, *Phys. Status Solidi Basic Res.* **2018**, *255*, 1800142.

- [17] J. Lim, D. Jeon, S. Lee, J. S. Yu, S. Lee, *Nanotechnology* **2020**, *31*, 115603.
- [18] X. Chen, B. Lei, Y. Zhu, J. Zhou, Z. Liu, W. Ji, W. Zhou, *Nanoscale* **2020**, *12*, 17005.
- [19] E. Liu, Y. Fu, Y. Wang, Y. Feng, H. Liu, X. Wan, W. Zhou, B. Wang, L. Shao, C. H. Ho, Y. S. Huang, Z. Cao, L. Wang, A. Li, J. Zeng, F. Song, X. Wang, Y. Shi, H. Yuan, H. Y. Hwang, Y. Cui, F. Miao, D. Xing, *Nat. Commun.* **2015**, *6*, 6991.
- [20] C. An, Z. Xu, W. Shen, R. Zhang, Z. Sun, S. Tang, Y. F. Xiao, D. Zhang, D. Sun, X. Hu, C. Hu, L. Yang, J. Liu, *ACS Nano* **2019**, *13*, 3310.
- [21] J. Ahn, K. Ko, J. Kyhm, H.-S. Ra, H. Bae, S. Hong, D.-Y. Kim, J. Jang, T. W. Kim, S. Choi, J.-H. Kang, N. Kwon, S. Park, B.-K. Ju, T.-C. Poon, M.-C. Park, S. Im, D. K. Hwang, *ACS Nano* **2021**, *15*, 17917.
- [22] X. Li, X. Wang, J. Hong, D. Liu, Q. Feng, Z. Lei, K. Liu, F. Ding, H. Xu, *Adv. Funct. Mater.* **2019**, *29*, 1906385.
- [23] H. Zhang, Y. Yu, X. Dai, J. Yu, H. Xu, S. Wang, F. Ding, J. Zhang, *Small* **2021**, *17*, 2102739.
- [24] K. Keyshar, Y. Gong, G. Ye, G. Brunetto, W. Zhou, D. P. Cole, K. Hackenberg, Y. He, L. Machado, M. Kabbani, A. H. C. Hart, B. Li, D. S. Galvao, A. George, R. Vajtai, C. S. Tiwary, P. M. Ajayan, *Adv. Mater.* **2015**, *27*, 4640.
- [25] K. Wu, B. Chen, S. Yang, G. Wang, W. Kong, H. Cai, T. Aoki, E. Soignard, X. Marie, A. Yano, A. Suslu, B. Urbaszek, S. Tongay, *Nano Lett.* **2016**, *16*, 5888.
- [26] X. Li, F. Cui, Q. Feng, G. Wang, X. Xu, J. Wu, N. Mao, X. Liang, Z. Zhang, J. Zhang, H. Xu, *Nanoscale* **2016**, *8*, 18956.
- [27] F. Cui, C. Wang, X. Li, G. Wang, K. Liu, Z. Yang, Q. Feng, X. Liang, Z. Zhang, S. Liu, Z. Lei, Z. Liu, H. Xu, J. Zhang, *Adv. Mater.* **2016**, *28*, 5019.
- [28] Q. He, J. Zhou, W. Tang, Y. Hao, L. Sun, C. Zhu, F. Xu, J. Chen, Y. Wu, Z. Wu, B. Xu, G. Liu, X. Li, C. Zhang, J. Kang, *ACS Appl. Mater. Interfaces* **2020**, *12*, 2862.
- [29] X. Li, X. Dai, D. Tang, X. Wang, J. Hong, C. Chen, Y. Yang, J. Lu, J. Zhu, Z. Lei, K. Suenaga, F. Ding, H. Xu, *Adv. Funct. Mater.* **2021**, *31*, 2102138.
- [30] R. He, J. A. Yan, Z. Yin, Z. Ye, G. Ye, J. Cheng, J. Li, C. H. Lui, *Nano Lett.* **2016**, *16*, 1404.
- [31] S. Wang, X. Wang, J. H. Warner, W. E. T. Al, *ACS Nano* **2015**, *9*, 5246.
- [32] H. Li, Y. Li, A. Aljarb, Y. Shi, L. J. Li, *Chem. Rev.* **2018**, *118*, 6134.
- [33] Y. C. Lin, H. G. Ji, L. J. Chang, Y. P. Chang, Z. Liu, G. Do Lee, P. W. Chiu, H. Ago, K. Suenaga, *ACS Nano* **2020**, *14*, 6034.
- [34] Y. Lin, H. Komsa, C. Yeh, L. I. N. E. T. Al, *ACS Nano* **2015**, *9*, 11249.
- [35] J. Dong, L. Zhang, F. Ding, *Adv. Mater.* **2019**, *31*, 1801583.
- [36] D. Wu, T. Min, J. Zhou, C. Li, G. Ma, G. Lu, M. Xia, Z. Gu, *Sci. Rep.* **2017**, *7*, 15166.
- [37] Z. Zhang, M. G. Lagally, *Science* **1997**, *276*, 377.
- [38] Y. Liu, S. Bhowmick, B. I. Yakobson, *Nano Lett.* **2011**, *11*, 3113.
- [39] X. Zhang, F. Zhang, Y. Wang, D. S. Schulman, T. Zhang, A. Bansal, N. Alem, S. Das, V. H. Crespi, M. Terrones, J. M. Redwing, *ACS Nano* **2019**, *13*, 3341.
- [40] S. Wang, Y. Yu, S. Zhang, S. Zhang, H. Xu, X. Zou, J. Zhang, *Matter* **2020**, *3*, 2108.
- [41] S. Wang, H. Sawada, C. S. Allen, A. I. Kirkland, J. H. Warner, *Nanoscale* **2017**, *9*, 13060.
- [42] M. C. Scharber, D. Mühlbacher, M. Koppe, P. Denk, C. Waldauf, A. J. Heeger, C. J. Brabec, *Adv. Mater.* **2006**, *18*, 789.
- [43] W. Hu, L. Lin, C. Yang, J. Dai, J. Yang, *Nano Lett.* **2016**, *16*, 1675.
- [44] D. Kim, H. J. Jung, I. J. Park, B. W. Larson, S. P. Dunfield, C. Xiao, J. Kim, J. Tong, P. Boonmongkolras, S. G. Ji, F. Zhang, S. R. Pae, M. Kim, S. B. Kang, V. Dravid, J. J. Berry, J. Y. Kim, K. Zhu, D. H. Kim, B. Shin, *Science* **2020**, *368*, 155.
- [45] Y. Zhou, E. Song, J. Zhou, J. Lin, R. Ma, Y. Wang, W. Qiu, R. Shen, K. Suenaga, Q. Liu, J. Wang, Z. Liu, J. Liu, *ACS Nano* **2018**, *12*, 4486.
- [46] Y. Liu, H. Li, J. Li, X. Ma, Z. Cui, D. Gao, Z. Tang, *J. Mater. Chem. A* **2021**, *9*, 14451.
- [47] Q. Zhang, L. Fu, *Chem* **2019**, *5*, 505.
- [48] L. Cao, Y. Yu, S. Huang, W. Yang, *Nano Lett.* **2014**, *14*, 553.
- [49] Y. Zhang, Q. Ji, G. F. Han, J. Ju, J. Shi, D. Ma, J. Sun, Y. Zhang, M. Li, X. Y. Lang, Y. Zhang, Z. Liu, *ACS Nano* **2014**, *8*, 8617.
- [50] J. Gao, L. Li, J. Tan, H. Sun, B. Li, J. Carlos, C. V. Singh, T. Lu, N. Koratkar, *Nano Lett.* **2016**, *16*, 3780.
- [51] N. Masurkar, N. K. Thangavel, L. M. R. Arava, *ACS Appl. Mater. Interfaces* **2018**, *10*, 27771.
- [52] Q. Ji, Y. Zhang, J. Shi, J. Sun, Y. Zhang, Z. Liu, *Adv. Mater.* **2016**, *28*, 6207.
- [53] D. Y. Chung, S. Park, P. P. Lopes, V. R. Stamenkovic, Y.-E. Sung, N. M. Markovic, D. Strmcnik, *ACS Catal.* **2020**, *10*, 4990.
- [54] B. E. Conway, E. Gileadi, H. G. Oswin, *Can. J. Chem.* **1963**, *41*, 2447.
- [55] S. Smidstrup, T. Markussen, P. Vancraeyveld, J. Wellendorff, J. Schneider, T. Gunst, B. Verstichel, D. Stradi, P. A. Khomyakov, U. G. Vej-Hansen, M. E. Lee, S. T. Chill, F. Rasmussen, G. Penazzi, F. Corsetti, A. Ojanperä, K. Jensen, M. L. N. Palsgaard, U. Martinez, A. Blom, M. Brandbyge, K. Stokbro, *J. Phys. Condens. Matter* **2020**, *32*, 015901.
- [56] G. Kresse, J. Furthmüller, *Comput. Mater. Sci.* **1996**, *6*, 15.
- [57] P. E. Blöchl, *Phys. Rev. B* **1994**, *50*, 17953.
- [58] A. Allouche, *J. Comput. Chem.* **2012**, *32*, 174.